International Journal of Nanomedicine

Dovepress

open access to scientific and medical research

Open Access Full Text Article

ORIGINAL RESEARCH

Mitochondria-Targeted Mesoporous Titanium Dioxide Nanoplatform for Synergistic Nitric Oxide Gas-Sonodynamic Therapy of Breast Cancer

Shuting Zuo, Yan Zhang, Zhenyu Wang, Jing Wang

Department of Breast Surgery, The Second Hospital of Jilin University, Changchun, People's Republic of China

Correspondence: Jing Wang, Department of Breast Surgery, The Second Hospital of Jilin University, Changchun, 130041, People's Republic of China, Tel/Fax +86 431-81136122, Email wangjing001@jlu.edu.cn

Background: Sonodynamic therapy (SDT) has rapidly advanced as a promising alternative to conventional photodynamic therapy owing to its preferable therapeutic depth. However, single-modal SDT exhibits limited efficacy due to the long-term hypoxia in tumors.

Method and Results: To address these issues, we proposed a synergistic SDT strategy that integrates mitochondrial targeting with nitric oxide (NO) gas therapy by using multifunctional nanoplatforms. The nanoplatform, which was named as T-mTNPs@L-Arg, was composed of mesoporous titanium dioxide loaded with the NO donor precursor L-arginine (L-Arg) and modified with triphenyl phosphonium (TPP), a mitochondria-targeting ligand. Therefore, T-mTNPs@L-Arg could efficiently concentrate into mitochondria and release NO gas as well as generate reactive oxygen species (ROS) with ultrasound stimulus. Importantly, the released NO gas exerted multiple synergies with SDT, including inducing NO poisoning, generating more lethal reactive nitrogen species (RNS) by reaction with ROS, and alleviating hypoxia through NO-mediated mitochondrial respiration inhibition. On account of the synergistic effects, T-mTNPs@L-Arg showed an outstanding SDT efficacy and a reduced side effect.

Conclusion: This work designed a nanoplatform to integrate mitochondria targeting, SDT and NO gas therapy, providing a new strategy for highly efficient breast cancer therapy.

Keywords: mitochondria-targeting, nitric oxide, sonodynamic therapy, titanium dioxide, synergistic

Introduction

Breast cancer has emerged as one of the mortal diseases threatening the lives of women all over the world.[1,2] The development of efficient and safe therapeutic modalities to prolong the survival of breast cancer patients and avoid the severe side effects of conventional therapies is an urgent task facing the medical community.[3,4] Sonodynamic therapy (SDT), which uses ultrasound (US) to trigger sonosensitizers to produce reactive oxygen species (ROS), is now at the center of attention due to its noninvasive characteristics and preferable therapeutic depth.[5,6] Nevertheless, currently, SDT is far from a radical cure for breast cancer due to its insufficient therapeutic efficiency.[7,8] On the one hand, singlet oxygen ($^1O_2$), as a highly toxic ROS generated by sonosensitizers, has an extremely short half-life with a limited diffusion distance, so it only performs well at the proximal site.[9,10] On the other hand, hypoxia, as a characteristic feature of most solid tumors, originates from the imbalance between the intake and consumption of O_2 due to abnormal metabolism and distorted vasculature and greatly compromises the efficacy and clinical translation of SDT.[11–13] In light of these findings, it has been recognized as a promising strategy to generate ROS at subcellular organelles and simultaneously modulate the tumor microenvironment for pursuit of improved SDT efficacy.

Mitochondria, as the energy center of cells, are widely distributed in the cytoplasm and maintain metabolic homeostasis.[14] Mitochondrial respiration includes mitochondrial aerobic respiration and aerobic glycolysis.[15] O_2 is mainly consumed by mitochondrial aerobic respiration-associated oxidative phosphorylation. Hyperactive O_2 metabolism

Received: 9 November 2021
Accepted: 25 February 2022
Published: 5 March 2022

of mitochondrial aerobic respiration in proliferating cancer cells is primarily responsible for the heterogeneous hypoxia of tumor tissues.[16] Therefore, mitochondria have been considered a vital target for cancer treatments, especially ROS-based therapies, because ROS easily enter mitochondria without hurdles, such as the karyotheca.[17] As an emerging field, gas therapy holds great promise for selective cancer therapy due to its "green" treatment.[18,19] Nitric oxide (NO), as the first gasotransmitter, has been found to have a multitude of physiological and pathological activities, including depleting intracellular glutathione (GSH), inducing NO poisoning and reacting with ROS to generate more lethal reactive nitrogen species (RNS).[20–23] Recent research has revealed that NO can remarkably decrease the O_2 consumption of cancer cells by inhibiting mitochondrial complex IV, an essential enzyme for the electron transport chain of mitochondrial respiration, which could alleviate the hypoxia in tumor tissues.[24] Thus, the strategy of combining SDT with gas therapy to generate NO promises to be a highly efficient and safe cancer therapy due to their synergistic effects.

To date, various NO donors, including NONOates (N-diazeniumdiolates), S-nitrosothiols (RSNOs), metal nitrosyls, and β-gal-NONOate (β-galactosyl-diazeniumdiolate), have been widely explored to release NO for disease treatment.[25,26] Among them, L-arginine (L-Arg), as a substrate for inducible nitric oxide synthases (iNOS), is a promising NO donor in response to endogenous hydrogen peroxide (H_2O_2) to produce NO.[27,28] However, the application of L-Arg is compromised by its poor cellular internalization and nontargeted biodistribution. Furthermore, similar to ROS, NO and RNS are very reactive and have difficulty reaching the mitochondria. Herein, it is urgent to develop nanocarriers to efficiently deliver L-Arg into mitochondria of cancer cells to simultaneously release ROS and NO. Mesoporous titanium dioxide nanoparticles (mTNPs) have attracted intensive interest as inorganic sonosensitizers because of their stable physicochemical properties and relatively good biocompatibility. Additionally, mTNPs possess an easily modified surface and unique mesopores, which endows them with excellent drug loading ability.[29,30] Triphenyl phosphonium (TPP), having three phenyl groups, is a common mitochondria-targeting ligand with positive charge to attract negatively charged mitochondria. Furthermore, TPP with sufficient lipophilicity could facilitate the process of transmembrane. The attractive performance of TPP in targeting mitochondria has been fully developed.[31]

In this work, mTNPs were synthesized and utilized to load L-Arg. Subsequently, TPP was modified on the surface of L-Arg loaded mTNPs (mTNPs@L-Arg) for mitochondria-targeting. The TPP-decorated mTNPs@L-Arg (T-mTNPs@L-Arg) could release L-Arg from the mesopores in a pH-responsive manner and produce NO upon the H_2O_2 stimulus from the tumor microenvironment. The generated NO effectively inhibited mitochondrial aerobic respiration, thus alleviating the hypoxic status of the tumor tissues. Additionally, T-mTNPs@L-Arg produced a large amount of ROS and more lethal RNS by the reaction of ROS with NO when exposed with US, which effectively destroyed the mitochondria of cancer cells. Based on the hypoxia relief, RNS generation and mitochondria targeting killing, T-mTNPs@L-Arg showed an enhanced SDT efficacy along with low side-effect. Collectively, our work provided a synergistic SDT strategy and demonstrated the potential applicability of T-mTNPs@L-Arg for highly efficient and safe breast cancer therapy (Scheme 1).

Methods

Synthesis of mTNPs

Our mTNPs were prepared using a sol-gel method. Briefly, 5 g of CTAB was dissolved in 100 mL of a mixture of water and ethanol (75 mL of distilled water and 25 mL of absolute ethanol). Then, 2 mL of titanium isopropoxide was added dropwise to the water and ethanol containing CTAB (CTAB/titanium isopropoxide molar ratio = 1/1) and reacted at 40 °C for 24 h. The resulting products were collected by centrifugation (8000 rpm, 10 min) and washed several times with ethanol. To remove CTAB, the prepared nanoparticles were dispersed in an ethanol solution of NH_4NO_3 (1.5% w/v) and refluxed at 105 °C for 24 h. Then, the mTNPs were obtained after centrifugation (8000 rpm, 10 min) and purified by washing with ethanol three time. To functionalize with amino groups, 1 mL of (3-aminopropyl) triethoxysilane (APTES) was added to a dimethylformamide (DMF) solution of mTNP. After stirring overnight, the mixture was heated to 80 °C for 2 h to obtain mTNPs with amino group functionalization. Then, 10 mg of amino-modified mTNPs were dispersed in the N, N-dimethylformamide (DMF) of succinic anhydride (50 mL, 2 wt%) and stirred at room temperature overnight. Then, the products were washed with ethanol three times, dried under vacuum and stored for subsequent experiments.

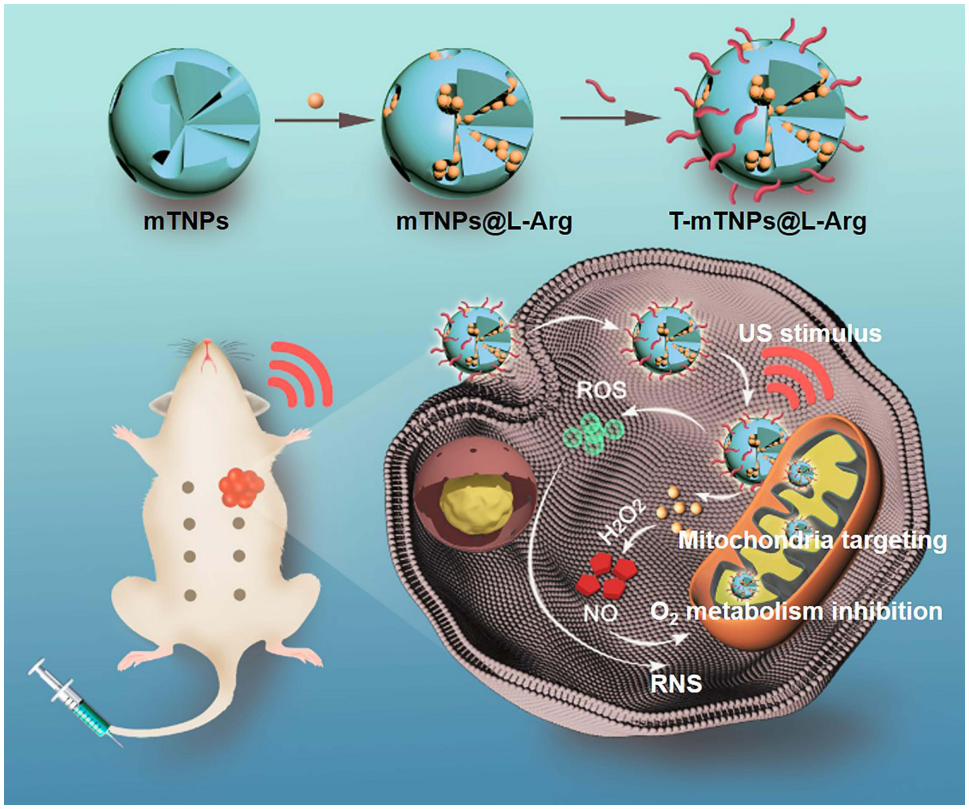

Scheme 1 Schematic illustration of mitochondria-targeted mesoporous titanium dioxide nanoparticles with L-arginine loading for synergistic nitric oxide gas-sonodynamic therapy.

L-Arg Loading

L-Arg stock solution was firstly prepared in water a concentration of 2 mg/mL (2 mg/mL). Then, 40 mg of carboxyl-modified mTNPs were dispersed in 20 mL deionized water under sonication to obtain mTNPs stock solution. Last, 20 mL L-Arg solution was mixed with 20 mL mTNPs solution, and the obtained mixture was shaken at 800 rpm at room temperature for 24 h followed by centrifugation. The loaded L-Arg was detected by the HPLC (Shimadzu LC-20AD, Japan, mobile phase: phosphate buffer/C2H3N (81/19, v/v); flow rate: 1.0 mL/min; detection wavelength: 210 nm) to determine the L-Arg release amount.

Modification of TPP

First, 35 mg of N-hydroxysulfosuccinimide (NHS) and 25 mg of 1-ethyl-3-(3-dimethylaminopropyl) carbodiimide (EDC) were added to a water solution of polyethylene glycol-conjugated TPP (10 mg/mL, 5 mL). After 2 h, 50 mg of mTNPs@L-Arg were added to the mixture for 24 h of reaction to obtain TPP-modified mTNPs (T-mTNPs).

L-Arg Release

To investigate the L-Arg release, 1 mg of T-mTNPs@L-Arg was dispersed into 2 mL PBS solution with different pH value (pH 7.4 and 5.5) and gently shaken at 100 rpm at 37 °C. At predetermined time points (0, 0.5, 1, 2, 3, 4, 5, 6, 9, 12, 24, 32, 48 and 72 h), the released L-Arg in the supernatant was collected by centrifugation (8000 r/min, 10 min) and subjected to measurement of HPLC (Shimadzu LC-20AD, Japan, mobile phase: phosphate buffer/C_2H_3N (81/19, v/v); flow rate: 1.0 mL/min; detection wavelength: 210 nm) to determine the L-Arg release amount.

NO Generation

To investigate the NO generation of T-mTNPs@L-Arg, 1 mg of T-mTNPs@L-Arg was placed in 2 mL PBS containing 0 μM or 100 μM H_2O_2 at different pH value (pH 7.4 and 5.5), and shaken at 100 rpm at 37 °C. At predetermined time points (0, 1, 2, 4, 6, 12, 24, 48 and 72 h), a NO detection reagent Griess reagent kit (Beyotime Biotechnology) was added to the supernatant to detect the amount of generated NO.

Cell Culture

Human breast cancer MCF-7 cells were purchased from the ATCC and cultured in RPMI 1640 medium with 10% fetal bovine serum. Normoxic MCF-7 cells were maintained under a normoxic atmosphere (74% N_2, 21% O_2 and 5% CO_2), and hypoxic MCF-7 cells were maintained under hypoxic conditions (90% N_2, 5% O_2 and 5% CO_2).

Cell Uptake

To investigate the cellular uptake of T-mTNPs@L-Arg, MCF-7 cells were cultured in 24-well plates at a density of 50,000 cells per well overnight and treated with FITC-labeled T-mTNPs@L-Arg and mTNPs@L-Arg (10 μg/mL) for 3 h. Then, these cells were washed and stained with LysoTraker Red and Hoechst 33258. Subsequently, these cells were observed by confocal laser scanning microscopy (CLSM; Olympus FV1000, Japan). For quantitative analysis, these cells incubated with FITC-labeled nanoparticles were washed, trypsinized, and resuspended subsequently and measured with a flow cytometer (BD Biosciences, Franklin Lakes, NJ, USA).

Mitochondria Targeting Evaluation

To evaluate the mitochondrial targeting of T-mTNPs@L-Arg, FITC-labeled T-mTNPs@L-Arg and mTNPs@L-Arg (10 μg/mL) were incubated with MCF-7 cells for 3 h. Then, the cells were washed with PBS three times and stained with Hoechst 33258 and MitoTracker for 30 min. Then, these cells were observed using confocal laser scanning microscopy (CLSM; Olympus FV1000; Olympus, Tokyo, Japan). To further quantitate the mitochondria-targeting efficacy, after 3 h of incubation with T-mTNPs@L-Arg and mTNPs@L-Arg, the cells were washed, trypsinized and resuspended. Then, the mitochondria in the cytoplasm were isolated using a mitochondria isolation kit. The fluorescence intensities of the FITC-labeled nanoparticles in the mitochondria were measured with a flow cytometer (BD Biosciences, Franklin Lakes, NJ, USA).

Cytochrome c Oxidase Activity Assessment

The activity of cytochrome c oxidase (CcO) was detected with a complex IV activity assay kit. Briefly, MCF-7 cells (2×10^6 cells per well) were incubated with mTNPs, T-mTNPs, mTNPs@ L-Arg or T-mTNPs@L-Arg (free L-Arg: 2.5 μg/mL, T-mTNPs@L-Arg: 50 μg/mL). After 12 h, the activity of CcO was measured following the manufacturer's protocol.

Intracellular Hypoxia Detection

MCF-7 cells were incubated with PBS, mTNPs, T-mTNPs, free L-Arg, mTNPs@L-Arg and T-mTNPs@L-Arg (L-Arg: 1 μg/mL) for 12 h. Then, the cells were covered with liquid paraffin for 6 h. Subsequently, all the cells were stained with hypoxia red detection reagent 1 (λex/λem = 488 nm/590 nm) for 30 min and subsequently washed with PBS for three times. The hypoxic condition of cells was detected by CLSM and flow cytometry.

Cytotoxicity Assessment and Intracellular Detection of ROS and RNS

MCF-7 cells were treated with mTNPs, T-mTNPs, mTNPs@L-Arg or T-mTNPs@L-Arg for 24 h and/or exposed to ultrasound (US) after 3 h of nanoparticle administration under normoxic (74% N_2, 21% O_2, and 5% CO_2) and hypoxic (90% N_2, 5% O_2, and 5% CO_2) conditions. The US at a frequency of 1 MHz at 1 W/cm^2 for 60 were applied for SDT according to the previous reports.[32–34] Then, the viabilities of the MCF-7 cells were determined with a CCK-8 assay kit. To examine intracellular ROS contents, DCFH-DA was added to the MCF-7 cells after various treatments and

coincubated for 20 min. To determine intracellular RNS contents, MCF-7 cells were incubated with DHR for 20 min. Then, the fluorescence signals of DCFH-DA and DHR were measured by flow cytometry.

Animal Experiments

Female nude mice weighing 20 g were bought from the Animal Experimental Center of Jilin University and kept in a traditional animal housing facility at the Second Hospital of Jilin University. All animal experimental protocols were approved by the Ethics Committee for the Use of Experimental Animals of the Second Hospital of Jilin University. Animal operations were in agreement with the National Institute of Health Guide for the Care and Use of Laboratory Animals.

In vivo Therapeutic Effect and Biosafety

An MCF-7 tumor-bearing nude mouse model was established by injecting 5×10^6 MCF-7 cells into the mammary fat pads of female nude mice. When the tumor volume reached about 250 mm^3, the mice were randomized into six groups: saline, US, T-mTNPs@L-Arg, T-mTNPs+US, mTNPs@L-Arg+US, and T-mTNPs@L-Arg+US. In the nanoparticle treatment groups, the MCF-7 tumor-bearing nude mice were intravenously injected with nanoparticles (10 mg/kg) every three days. Additionally, the tumor sites were irradiated with a US (1 MHz, 1 W/cm^2) for 60s after 6h injection of nanoparticles or PBS in the US treatment groups. Tumor growth was recorded using a digital caliper at 2 days post-administration, and tumor volumes were calculated using the following equation: volume = length × $width^2$ × 0.52. All treatments were terminated on the 23rd day. The tumors were subsequently harvested from mice and weighed. The livers, spleens, kidneys, lungs and hearts of the mice were stained with hematoxylin-eosin. Blood was collected from the mice and used to assess the biochemical parameters.

Immunohistochemistry

To investigate the hypoxic status of tumor tissues, the tumors was harvested on the 6th day and embedded in paraffin. Then, rabbit polyclonal HIF-1α antibody were used as the primary antibody for the staining of HIF-1α in tumor tissues. To evaluate intratumoral apoptosis, the tumors were subjected to the fluorescence terminal deoxynucleotidyl transferase deoxyuridine triphosphate nick end labeling (TUNEL) assay.

Statistical Analysis

Student's *t*-test was used to analyze the differences between two groups. The differences among more than two groups were analyzed by one-way analysis of variance. A value of $p < 0.05$ represents a statistically significant difference.

Results and Discussion

The mTNPs were synthesized according to the conventional sol-gel method using titanium isopropylate as a precursor and cetrimonium bromide (CTAB) as a template. Then, CTAB was extracted by ion exchange in ethanolic HCl to form mesoporous scaffolds. The transmission electron microscopy (TEM) image clearly revealed that the mTNPs had a uniform spherical morphology with a diameter of ~50 nm (Figure 1A). Dynamic light scattering (DLS) analysis of aqueous mTNP dispersions further supported the TEM observations (Figure 1B). The surface areas and pore sizes of the mTNPs were characterized by N_2 adsorption/desorption isotherms. The isotherms were classified as Type IV isotherms without hysteresis, indicating the well-defined mesopores of mTNPs (Figure 1C). The Brunauer-Emmett-Teller (BET) surface area, Barrett−Joyner−Halenda (BJH) pore size and total pore volume were calculated to be 521.2 $m^2\ g^{-1}$, 4.1 nm and 0.46 $cm^3\ g^{-1}$, respectively (Figure 1D). To load L-Arg, the surface of mTNPs were first functionalized with amine groups by the direct addition of APTS to the reaction solution, and then reacted with succinic anhydride to prepare carboxyl-functionalized mTNPs. The obvious change in zeta potential before and after the reaction indicated successfully functionalized process of the amine and carboxyl groups (Figure S1). Then, L-Arg was loaded into the mesopores of mTNPs and the drug loading content was measured to be 5.1% by HPLC. For mitochondrial targeting, TPP-polyethylene glycol (PEG) amine was subsequently conjugated with the carboxylate group on the mTNPs surface. The UV−vis confirmed the successful TPP conjugation, as indicated by the characteristic absorption peak at 270 nm in the T-mTNPs

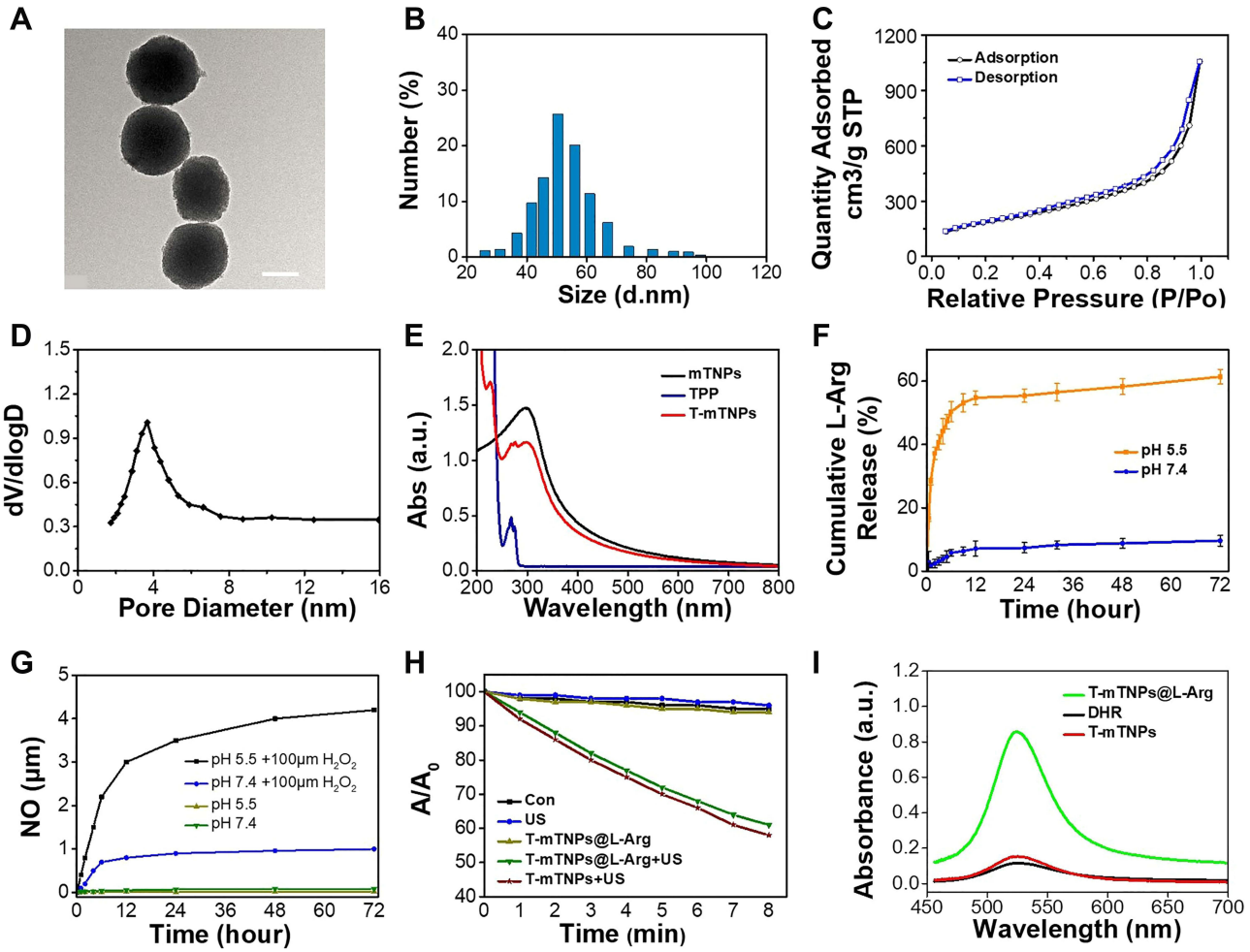

Figure 1 Characterization of T-mTNPs: (**A**) TEM images of mTNPs, scale bar=30 nm, (**B**) DLS analysis of mTNPs, (**C**) N_2 adsorption/desorption isotherms of mTNPs, (**D**) Pore size distribution of mTNPs, (**E**) UV–vis absorption spectra, (**F**) L-Arg release profiles of T-mTNPs@L-Arg under different pH value, (**G**) Cumulative NO generation at different pH at the presence or absence of H_2O_2, (**H**) ROS generation detected by DPBF probe, (**I**) fluorescence spectrum of $ONOO^-$ detected by DHR probe.

(Figure 1E). The drug release profiles of T-mTNPs@L-Arg were subsequently investigated in PBS solution at different pH value. As shown in Figure 1F, more than 60% of L-Arg was released from T-mTNPs@L-Arg at pH 5.5 in contrast to less than 10% L-Arg release at pH 7.4 within 24 h, indicating the pH-responsive drug release property of T-mTNPs@L-Arg. Furthermore, T-mTNPs@L-Arg showed a constant particle size distribution for 5 days in pure water and cell medium, whereas mTNPs@L-Arg aggregated in the cell culture medium, which suggested the stability of the nanoparticles was improved after PEGylation (Figure S2). The NO generation contains two steps: (1) the release of L-Arg from T-mTNPs@L-Arg, and (2) the reaction of L-Arg with endogenously H_2O_2 to generate NO. Thus, we investigated the NO production of T-mTNPs@L-Arg in the media mimicking intracellular ROS conditions in tumor micro-environment at different pH value. As shown in Figure 1G, rare NO was produced without H_2O_2 at pH 5.5 or 7.4, whereas significant NO generation was detected in the presence of H_2O_2. Additionally, T-mTNPs@L-Arg produced obviously more NO at pH 5.5 than that at pH 7.4, which was consistent with the drug release. These results indicated that T-mTNPs@L-Arg could produce NO in response to the tumor microenvironment, which might reduce the adverse effect of NO poisoning in normal tissues.

To explore the potential of T-mTNPs@L-Arg as sonosensitizers, the production of reactive oxide species (ROS) was detected under the exposure of ultrasound (US) by 1,3-diphenyl isobenzofuran (DPBF), a typical ROS analytical reagent. As shown in Figure 1H, the absorption value of DPBF in the T-mTNPs@L-Arg and T-mTNPs groups significantly decreased with the extension of US treatment time, indicating that T-mTNPs@L-Arg and T-mTNPs could generate

significant ROS after US stimulus. We hypothesized that ROS could react with the simultaneously released NO to generate more poisonous reactive nitrogen species (RNS). To verify this, T-mTNPs or T-mTNPs@L-Arg was exposed with US in the H_2O_2 solution at pH 5.5, and the RNS generation was detected by a dihydrorhodamine 123 (DHR), a RNS detection reagent that reacts with RNS to emit strong green fluorescence. As shown in Figure 1I, the fluorescence signals of DHR remained unchanged in the T-mTNPs group in comparison with the control group, whereas the T-mTNPs@L-Arg group induced a significant increase in fluorescence. These results indicated that T-mTNPs@L-Arg plus US could generate RNS due to the simultaneous generation of ROS and NO, which might be beneficial to enhancing the SDT effects because RNS are more lethal.

We next investigated the cellular internalization of FITC-labeled T-mTNPs@L-Arg and mTNPs@L-Arg in MCF-7 cells. As shown in Figure S3A, both T-mTNPs@L-Arg and mTNPs@L-Arg was observed to partly colocalize with Lysotracker Red, indicating that these nanoparticles could be taken up by MCF-7 cells, and some nanoparticles entered the lysosomes whereas others were present in the cytoplasm. Additionally, T-mTNPs@L-Arg and mTNPs@L-Arg showed a similar cellular uptake efficiency (Figure S3B), and the co-localization coefficient of lysosomes with T-mTNPs@L-Arg was 0.32, which was approximate to that with mTNPs@L-Arg (0.30). To investigate the mitochondria-targeting capacity of T-mTNPs, the localization of T-mTNPs@L-Arg and mTNPs@L-Arg with mitochondria was also observed cells using CLSM. As shown in Figure 2A, more T-mTNPs@L-Arg showed a high colocalization with MitoTracker Red (co-localization coefficient = 0.47). In contrast, less mTNPs@L-Arg concentrated in the mitochondria, and the co-localization coefficient of mTNPs@L-Arg with mitochondria was only 0.11. To further confirm the successful targeting of T-mTNPs@L-Arg to the mitochondria, mitochondria were isolated from MCF-7 cells after treated with T-mTNPs@L-Arg and mTNPs@L-Arg, and the fluorescence signals of the isolated mitochondria were detected by

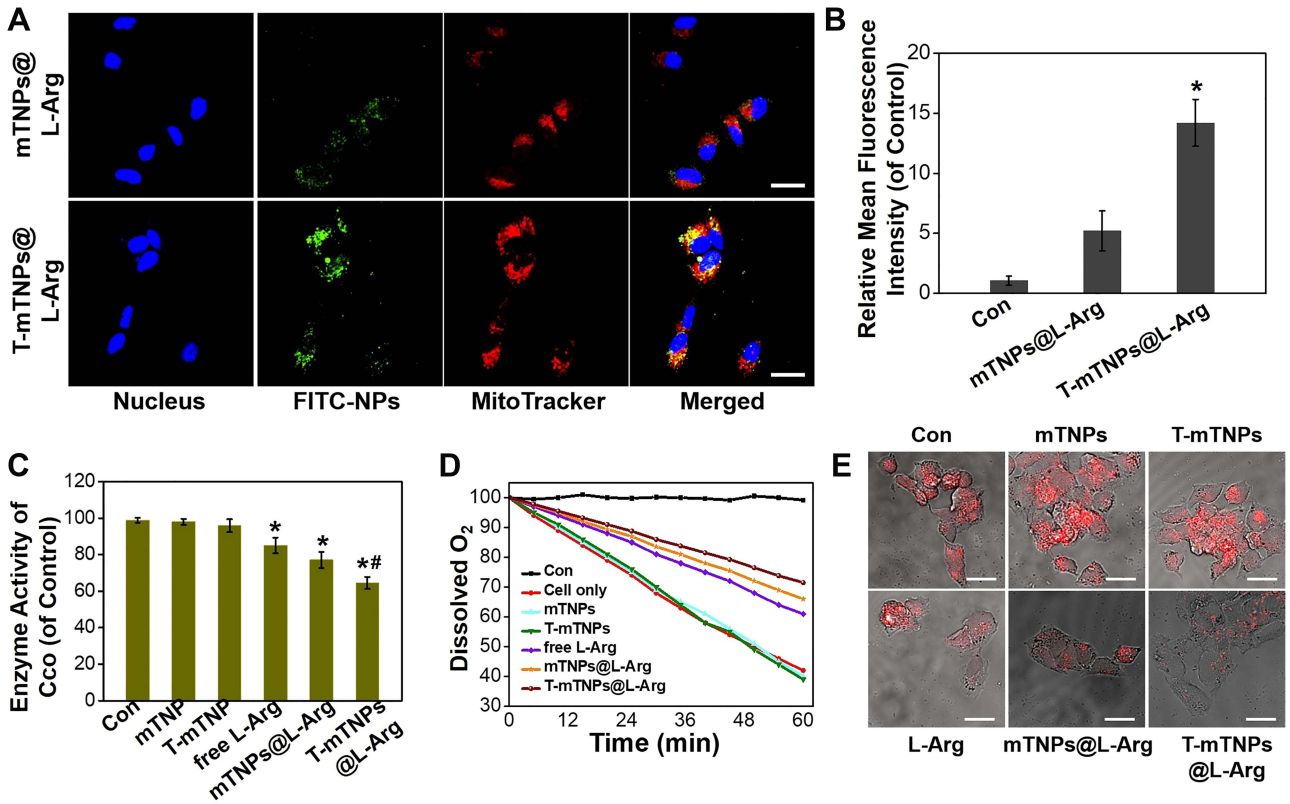

Figure 2 Mitochondria targeting and hypoxia relief: (**A**) Confocal microscope images of MCF-7 cells after incubated with FITC-labeled T-mTNPs@L-Arg and mTNPs@L-Arg and stained with Hoechst 33258 and MitoTracker, scale bar=10 nm (**B**) FITC fluorescence intensity of isolated mitochondria from MCF-7 cells after incubated with FITC-labeled T-mTNPs@L-Arg and mTNPs@L-Arg. The data are presented as the mean ± S.D. (n = 4). *p < 0.05 versus the mTNPs@L-Arg (**C**) Activity of Cco after various treatments. The data are presented as the mean ± S.D. (n = 4). *p < 0.05 versus the control groups, #p < 0.05 versus mTNPs@L-Arg. (**D**) Relative dissolved oxygen content in the cell medium of various groups. (**E**) Hypoxic status of MCF-7 cells detected by hypoxia red detection reagent I, scale bar=10 nm.

FACS.As shown in Figure 2B, a high FITC fluorescence intensity was detected in the T-mTNPs@L-Arg-treated group, whereas remarkably less FITC signals were found in the mTNPs@L-Arg-treated group. These results further confirmed the excellent mitochondria-targeting capability of the T-mTNPs@L-Arg.

NO has been demonstrated to inhibit mitochondrial complex IV through competitive binding with the O_2 binding sites of cytochrome c oxidase (Cco), which could restrain hypoactive O_2 metabolism. Given the mitochondria-targeted capacity and NO release properties, we expected that T-mTNPs@ L-Arg could decrease cellular Cco activity to retard the O_2 consumption of cancer cells. Thus, the activity of Cco in MCF-7 cells was measured after incubation with mTNPs, T-mTNPs, free L-Arg, mTNPs@L-Arg and T-mTNPs@L-Arg for 12 h using a complex IV activity assay kit. As shown in Figure 2C, the cellular Cco after treatment with mTNPs and T-mTNPs maintained good activity, indicating that T-mTNPs without L-Arg loading have no inhibitory effect on the activity of Cco. As expected, the activity of Cco was obviously decreased in the free L-Arg, mTNPs@L-Arg and T-mTNPs@L-Arg treatment groups, confirming the inhibitory effects of L-Arg and L-Arg-loaded particles on mitochondrial aerobic respiration. Furthermore, T-mTNPs@L-Arg showed remarkably greater inhibition of the activity of Cco than mTNPs@L-Arg and free L-Arg, which was due to the mitochondria-targeted release of NO by T-mTNPs@L-Arg. Cco is responsible for 90% of O_2 consumption; thus, we measured the amount of dissolved oxygen in airtight cell medium containing MCF-7 cells using an oxygen electrode. As shown in Figure 2D, MCF-7 cells treated with mTNPs and T-mTNPs induced a sharp decrease in dissolved O_2, which was similar to the cells without any treatment. In the cells treated with free L-Arg, mTNPs@L-Arg and T-mTNPs@L-Arg, the consumption of dissolved O_2 was significant retarded. Specifically, cells treated with T-mTNPs@L-Arg showed the slowest O_2 consumption, and the amount of dissolved O_2 decreased to only 71.5%. These results indicated that T-mTNPs@L-Arg could restrict the O_2 consumption of cancer cells better than mTNPs@L-Arg due to the mitochondria-targeted release of NO. We also detected the intracellular hypoxia status of MCF-7 cells in airtight environment after various treatments using hypoxia red detection reagent l. As shown in Figure 2E, cells treated with mTNPs and T-mTNPs exhibited the intense fluorescence signals of hypoxia originated from O_2 consumption, similar to cells treated with PBS. In contrast, hypoxic fluorescence signals of MCF-7 cells were decreased after treatment with free L-Arg, mTNPs@L-Arg and T-mTNPs@L-Arg, indicating the decrease of O_2 consumption in MCF-7 cells. Furthermore, the fluorescence signal in the T-mTNPs@L-Arg-treated group was the lowest than those other treatment groups. Consistent results were detected by FACS (Figure S4). The results confirmed that T-mTNPs@L-Arg with mitochondria-targeting possessed a better ability to alleviate tumor hypoxia than the nontargeted mTNPs@L-Arg.

Given the mitochondrial targeting ability of T-mTNPs@L-Arg, we verified the SDT-induced destruction of mitochondria using Rhodamine 123, a fluorescent indicator, to evaluate mitochondrial dysfunction. As shown in Figures 3A and S5, without US irradiation, MCF-7 cells treated with T-mTNPs@L-Arg showed high green fluorescence signals from rhodamine 123, similar to the control group, indicating that the mitochondria in these MCF-7 cells were not destroyed. After exposure to US, the green fluorescence signals in the cells after treatment with T-mTNPs were remarkably lower than those in the cells after treatment with mTNPs, suggesting that mitochondria-targeted SDT could induce more mitochondrial damage. Additionally, T-mTNPs@L-Arg showed a stronger effect on destroying mitochondria, which was likely because of the generation of more lethal RNS.

Subcellular localization of T-mTNPs@L-Arg did not only alleviate hypoxia, but also improved the sonodynamic damage degree of mitochondria, which was expected to exert an efficient synergetic SDT effect. Thus, we evaluated the in vitro therapeutic efficacy of T-mTNPs@L-Arg using a CCK-8 assay. As shown in Figure 3B, negligible cytotoxicity was measured in MCF-7 cells after treated with mTNPs and T-mTNPs, indicating the good biocompatibility of our T-mTNPs. Additionally, mTNPs@L-Arg and T-mTNPs@L-Arg showed slight cytotoxicity toward MCF-7 cells, which was possibly due to NO poisoning of the cancer cells induced by the release of NO gas. After exposure to US, all of the nanoparticle-treated cells displayed concentration-dependent cytotoxicity (Figure 3C). Additionally, T-mTNPs@L-Arg displayed the strongest therapeutic effect compared with mTNPs, mTNPs@L-Arg and T-mTNPs, which was attributed to mitochondrial targeting and the synergistic effect of NO gas and ROS. Considering the ubiquitous hypoxic region in tumor tissue, we evaluated the SDT efficacy of T-mTNPs@L-Arg toward MCF-7 cells in hypoxic condition. As shown in Figure 3D, the therapeutic effects of T-mTNPs combined with US was greatly compromised under hypoxic conditions. Comparatively, T-mTNPs@L-Arg plus US maintained a good killing effect toward hypoxic MCF-7 cells, confirming the

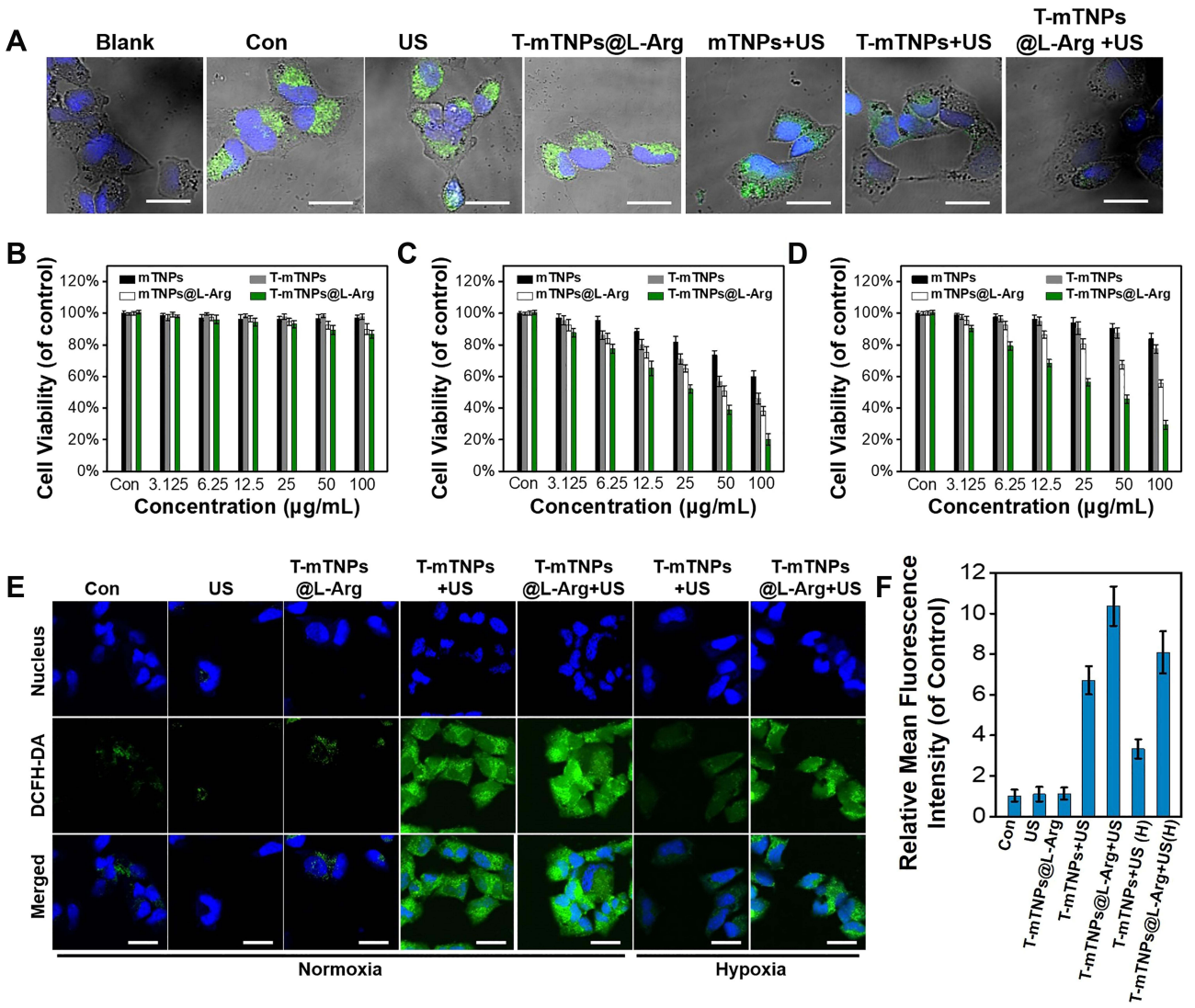

Figure 3 In Vitro SDT efficacy of T-mTNPs@L-Arg. (**A**) The destruction of mitochondria in MCF-7 cells after various treatments detected by CLSM, scale bar=10 nm. Cytotoxicity of different nanoparticles towards MCF-7 cells in the absence (**B**) or presence (**C**) of US stimulus. (**D**) Cell viability of hypoxic MCF-7 cells after treated with different nanoparticles in the presence of US. (**E**) CLSM images of MCF-7 cells stained with DCFH-DA in various groups, scale bar=10 nm. (**F**) ROS generation in various groups detected by FACS ("H" represents hypoxia). The data are presented as the mean ± S.D. (n = 4).

ability of T-mTNPs@L-Arg as sonosensitizers to treat hypoxic tumors. To further clarify the mechanism, we verified the intracellular ROS and RNS generation using the common ROS probes 2′,7′-dichlorofluorescein diacetate (DCFH-DA) and RNS probes DHR. As shown in Figure 3E and F, neither sole US nor T-mTNPs@L-Arg could induce intracellular ROS generation. In contrast, a significant improvement in ROS signals was detected after treatment with T-mTNPs, and T-mTNPs@L-Arg under the US irradiation. Additionally, the production of ROS in the T-mTNP treatment groups was greatly restricted in hypoxic MCF-7 cells, whereas T-mTNPs@L-Arg still maintained considerable ROS generation efficiency due to hypoxia relief by the generated NO in the mitochondria. Additionally, rare intracellular RNS was detected in T-mTNPs plus US or T-mTNPs@L-Arg groups, whereas T-mTNPs@L-Arg plus US resulted in a significant production of RNS in MCF-7 cells, which further confirmed the synergistic effects of NO gas with SDT (Figure S6).

Inspired by the excellent therapeutic effects in vitro, we evaluated the antitumor effects of T-mTNPs@L-Arg in vivo using an MCF-7 tumor-bearing nude mouse model. The biodistribution of Cy5.5-labeled T-mTNPs@L-Arg was first measured after intravenous injection. Figure 4A showed that T-mTNPs@L-Arg was predominantly distributed in the tumor tissue, liver, spleen and kidney. The accumulation of T-mTNPs@L-Arg peaked at 6 h after intravenous

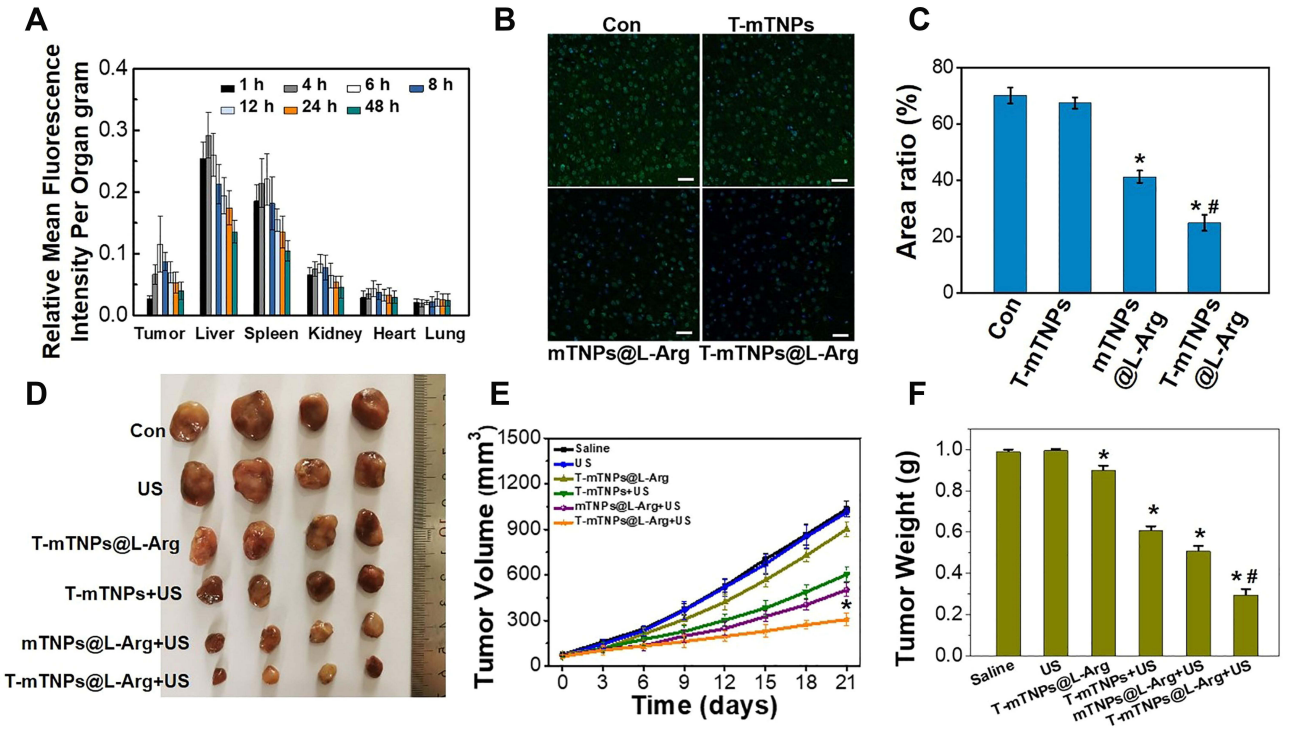

Figure 4 In Vivo SDT efficacy of T-mTNPs@L-Arg. (**A**) Biodistribution of T-mTNPs@L-Arg in MCF-7 tumor-bearing mice after intravenous injection at different time points. (**B**) Immunofluorescence images of tumors in various treatments on day 6. Tumor hypoxia was detected by Pimonidazole binding of HIF-1α antibody staining, scale bar=50 nm. (**C**) FACS assay of hypoxic area in tumor tissues. *p < 0.05 versus the control groups, #p < 0.05 versus mTNPs@L-Arg. (**D**) Tumor photographs. (**E**) Tumor volume. *p < 0.05 versus mTNPs@L-Arg. (**F**) Tumor weight. *p < 0.05 versus the control groups, #p < 0.05 versus mTNPs@L-Arg. All the data are presented as the mean ± S.D. (n = 4).

administration, followed by a gradual decrease. Then, we investigated the ability of T-mTNPs@L-Arg to alleviate hypoxia in tumors. As shown in Figure 4B and C, the fluorescence signals of hypoxia in the T-mTNP treatment group were similar to that in the saline control group, which indicated that T-mTNPs without L-Arg loading have little effect on hypoxic relief. In contrast, hypoxia-associated fluorescence signals decreased after intravenous injection with mTNPs@L-Arg and T-mTNPs@L-Arg, while T-mTNPs@L-Arg showed a better effect on the decrease in the hypoxic region due to mitochondrial targeting. The hypoxia relief caused by T-mTNPs@L-Arg would be conducive to enhancing SDT efficiency. To evaluate the antitumor effects, tumor-bearing mice models were randomized into six groups (saline, US, T-mTNPs@L-Arg, T-mTNPs+US, mTNPs@L-Arg+US, and T-mTNPs@L-Arg+US) and intravenously injected with nanoparticles every 3 days and/or exposed to US after 6 h of administration, and the experiment was terminated on Day 23. As shown in Figure 4D–F, the tumors in the T-mTNP@L-Arg group grew quickly, indicating that T-mTNPs@L-Arg with US had a small antitumor effect. Tumor growth inhibition was observed in the T-mTNPs+US, mTNPs@L-Arg+US, and T-mTNPs@L-Arg+US groups, which confirmed the SDT efficacy of our nanoparticles. Furthermore, the T-mTNP@L-Arg+US group showed the highest decreases in the relative volume and weight in comparison to the mTNPs@L-Arg+US or T-mTNPs+US groups. These results indicated that mitochondria-targeted combination therapies have better antitumor efficiency than nontargeted combination therapies or SDT alone. In addition, we performed TUNEL immunostaining to evaluate cell apoptosis in tumor sections. As shown in Figure S7, negligible apoptotic fluorescence signals were observed in the US and T-mTNPs@L-Arg groups. T-mTNPs and mTNPs@L-Arg induced apoptosis under US stimulus. As expected, the highest level of apoptosis was observed in the T-mTNPs@L-Arg+US group, which was consistent with the results of the tumor growth curve and tumor weights. These results indicated that the efficient tumor inhibition originated from the SDT-induced apoptosis of the breast cancer cells.

Biosafety is a prerequisite for the clinical translation of nanoparticles. Thus, we examined the body weights, serum chemistry indices and histology of the major organs to evaluate the systemic toxicity of the treatments. In comparison to the saline control group, no weight loss was observed in the treatment groups (Figure 5A). The levels of the serum

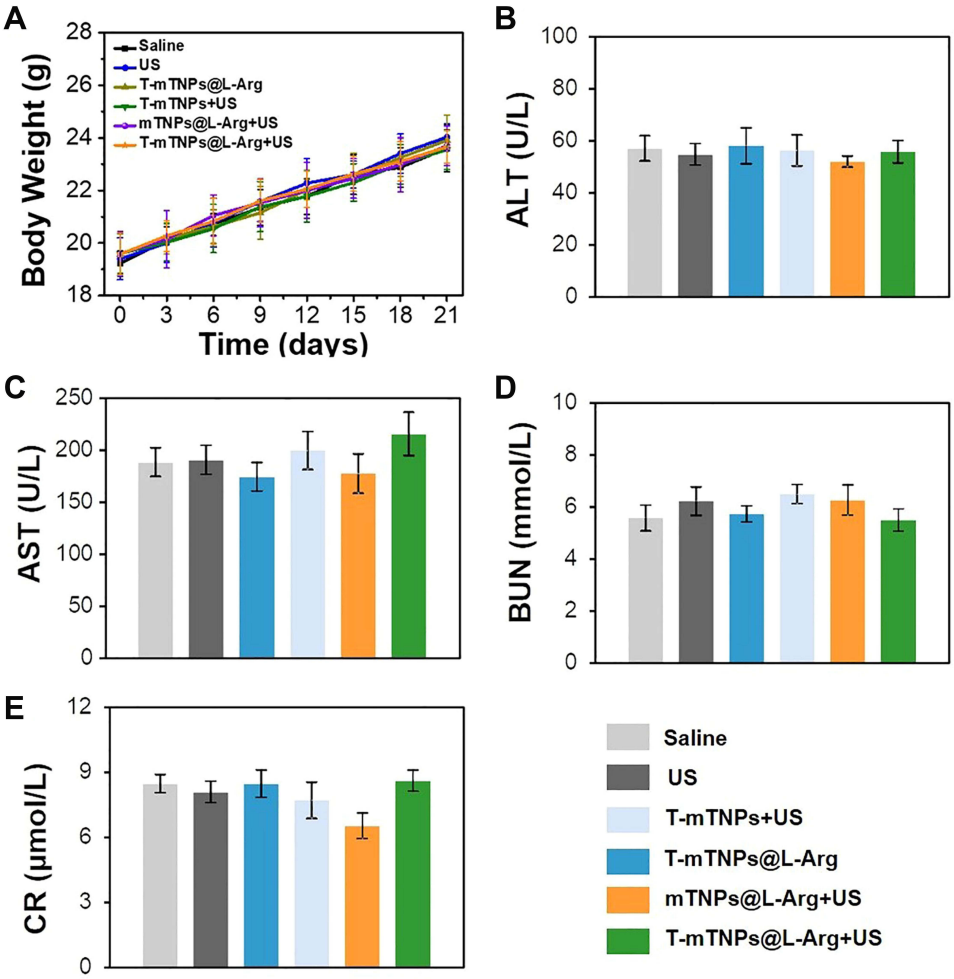

Figure 5 Evaluation of the systemic toxicity: (**A**) body weight. (**B–E**) blood biochemistry indicators include (**B**) alanine aminotransferase (ALT), (**C**) aspartate aminotransferase (AST), (**D**) blood urea nitrogen (BUN), and (**E**) creatinine (CRE). Data are presented as the mean ± S.D. (n = 4).

chemistry indices, including ALB, ALT, AST, BUN and CRE, did not remarkably change in any of the treatment groups (Figure 5B–E). Furthermore, H&E staining of the liver, spleen, kidney, lung, and heart indicated the absence of pathological damage in the major organs during treatment (Figure 6). Collectively, these results confirmed the good biosafety of T-mTNPs@L-Arg.

Conclusion

In summary, we designed mesoporous titanium dioxide nanoplatforms (T-mTNPs@L-Arg) by loading L-Arg and modifying with triphenyl phosphine (TPP) for mitochondria targeting and nitric oxide (NO) gas combined sonodynamic therapy. Due to the TPP modification, the T-mTNPs@NO were internalized into the cytoplasm and preferred to bind with the mitochondria. Upon activation by US, the T-mTNPs@L-Arg produced a large amount of ROS to induce mitochondrial damage. Furthermore, T-mTNPs@L-Arg could release L-Arg in a pH-responsive manner and generate NO gas in a H_2O_2-containing microenvironment, which not only generated more lethal RNS by the reaction of ROS with NO, but also alleviated hypoxia through NO inhibition of mitochondrial aerobic respiration-related O_2 metabolism. Based on these synergistic effects, T-mTNPs@L-Arg exhibited excellent SDT efficacy along with low systemic toxicity. Overall, our research provides new insight into advancing the development of highly efficient SDT to treat cancer.

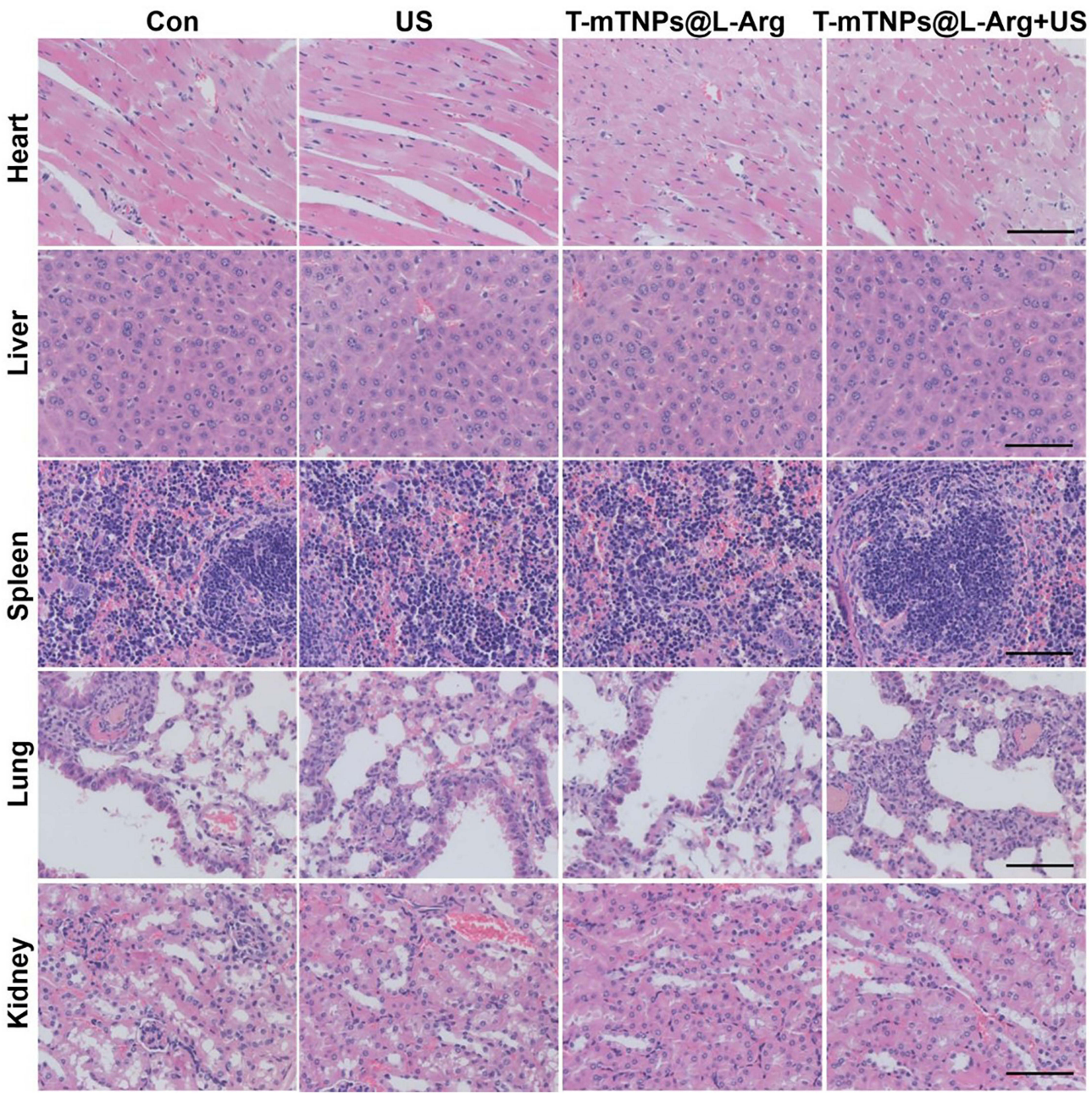

Figure 6 H&E staining images of the heart, liver, spleen, lung, and kidney from mice in various treatments, scale bar=100 nm.

Data Sharing Statement

Supplementary Materials are linked to this paper and supporting data are available from the authors.

Acknowledgment

The study was supported by the Finance Department Program of Jilin Province (2020SCZT028).

Disclosure

The authors report no conflicts of interest in this work.

References

1. Kurian AW, Ward KC, Howlader N, et al. Genetic testing and results in a population-based cohort of breast cancer patients and ovarian cancer patients. *J Clin Oncol*. 2019;37(15):1305. doi:10.1200/JCO.18.01854
2. Waks AG, Winer EP. Breast cancer treatment: a review. *JAMA*. 2019;321(3):288–300. doi:10.1001/jama.2018.19323
3. Jain V, Kumar H, Anod HV, et al. A review of nanotechnology-based approaches for breast cancer and triple-negative breast cancer. *J Control Release*. 2020;326:628–647. doi:10.1016/j.jconrel.2020.07.003
4. Khoobchandani M, Katti KK, Karikachery AR, et al. New approaches in breast cancer therapy through green nanotechnology and nano-ayurvedic medicine–pre-clinical and pilot human clinical investigations. *Int J Nanomedicine*. 2020;15:181. doi:10.2147/IJN.S219042
5. Pan X, Wang H, Wang S, et al. Sonodynamic therapy (SDT): a novel strategy for cancer nanotheranostics. *Sci China Life Sci*. 2018;61(4):415–426. doi:10.1007/s11427-017-9262-x
6. Zhu P, Chen Y, Shi J. Nanoenzyme-augmented cancer sonodynamic therapy by catalytic tumor oxygenation. *ACS Nano*. 2018;12(4):3780–3795. doi:10.1021/acsnano.8b00999
7. Xu T, Zhao S, Lin C, Zheng X, Lan M. Recent advances in nanomaterials for sonodynamic therapy. *Nano Res*. 2020;13(11):2898–2908.
8. Serpe L, Foglietta F, Canaparo R. Nanosonotechnology: the next challenge in cancer sonodynamic therapy. *Nanotechnol Rev*. 2012;1(2):173–182. doi:10.1515/ntrev-2011-0009
9. Li X, Gao M, Xin K, et al. Singlet oxygen-responsive micelles for enhanced photodynamic therapy. *J Control Release*. 2017;260:12–21. doi:10.1016/j.jconrel.2017.05.025
10. Midden WR, Wang SY. Singlet oxygen generation for solution kinetics: clean and simple. *J Am Chem Soc*. 1983;105(13):4129–4135. doi:10.1021/ja00351a001
11. McEwan C, Owen J, Stride E, et al. Oxygen carrying microbubbles for enhanced sonodynamic therapy of hypoxic tumours. *J Control Release*. 2015;203:51–56. doi:10.1016/j.jconrel.2015.02.004
12. Chen J, Luo H, Liu Y, et al. Oxygen-self-produced nanoplatform for relieving hypoxia and breaking resistance to sonodynamic treatment of pancreatic cancer. *ACS Nano*. 2017;11(12):12849–12862. doi:10.1021/acsnano.7b08225
13. Fu J, Li T, Zhu Y, Hao Y. Ultrasound-activated oxygen and ROS generation nanosystem systematically modulates tumor microenvironment and sensitizes sonodynamic therapy for hypoxic solid tumors. *Adv Funct Mater*. 2019;29(51):1906195. doi:10.1002/adfm.201906195
14. Fulda S, Galluzzi L, Kroemer G. Targeting mitochondria for cancer therapy. *Nat Rev Drug Discov*. 2010;9(6):447–464.
15. Orang AV, Petersen J, McKinnon RA, Michael MZ. Micromanaging aerobic respiration and glycolysis in cancer cells. *Mol Metab*. 2019;23:98–126. doi:10.1016/j.molmet.2019.01.014
16. Moreno-Sanchez R, Marin-Hernandez A, Saavedra E, Pardo JP, Ralph SJ, Rodriguez-Enriquez S. Who controls the ATP supply in cancer cells? Biochemistry lessons to understand cancer energy metabolism. *Int J Biochem Cell Biol*. 2014;50:10–23. doi:10.1016/j.biocel.2014.01.025
17. Sang M, Luo R, Bai Y, et al. Mitochondrial membrane anchored photosensitive nano-device for lipid hydroperoxides burst and inducing ferroptosis to surmount therapy-resistant cancer. *Theranostics*. 2019;9(21):6209. doi:10.7150/thno.36283
18. Tiemuer A, Yu H, Zhao C, et al. Nitroso-caged upconversion luminescent prodrug: near infrared light-activatable NO nano-donor for gas therapy. *Chem Eng J*. 2022;430:132858.
19. Chen L, Zhou S-F, Su L, Song J. Gas-mediated cancer bioimaging and therapy. *ACS nano*. 2019;13(10):10887–10917. doi:10.1021/acsnano.9b04954
20. Fan W, Yung BC, Chen X. Stimuli-responsive NO release for on-demand gas-sensitized synergistic cancer therapy. *Angew Chem Int Ed*. 2018;57(28):8383–8394. doi:10.1002/anie.201800594
21. Deng Y, Jia F, Chen S, et al. Nitric oxide as an all-rounder for enhanced photodynamic therapy: hypoxia relief, glutathione depletion and reactive nitrogen species generation. *Biomaterials*. 2018;187:55–65. doi:10.1016/j.biomaterials.2018.09.043
22. Wan -S-S, Zeng J-Y, Cheng H, Zhang X-Z. ROS-induced NO generation for gas therapy and sensitizing photodynamic therapy of tumor. *Biomaterials*. 2018;185:51–62. doi:10.1016/j.biomaterials.2018.09.004
23. Wang Y, Huang X, Tang Y, et al. A light-induced nitric oxide controllable release nano-platform based on diketopyrrolopyrrole derivatives for pH-responsive photodynamic/photothermal synergistic cancer therapy. *Chem Sci*. 2018;9(42):8103–8109. doi:10.1039/C8SC03386B
24. Xiang Q, Qiao B, Luo Y, et al. Increased photodynamic therapy sensitization in tumors using a nitric oxide-based nanoplatform with ATP-production blocking capability. *Theranostics*. 2021;11(4):1953. doi:10.7150/thno.52997
25. Yang Y, Huang Z, Li L. Advanced nitric oxide donors: chemical structure of NO drug, NO nanomedicines and biomedical applications. *Nanoscale*. 2021;13(2):444–459.
26. Soto RJ, Yang L, Schoenfisch MH. Functionalized mesoporous silica via an aminosilane surfactant ion exchange reaction: controlled scaffold design and nitric oxide release. *ACS Appl Mater Interfaces*. 2016;8(3):2220–2231. doi:10.1021/acsami.5b10942
27. Yang H, Jiang F, Zhang L, et al. Multifunctional l-arginine-based magnetic nanoparticles for multiple-synergistic tumor therapy. *Biomater Sci*. 2021;9(6):2230–2243. doi:10.1039/D0BM01932A
28. Han C, Yu Q, Jiang J, et al. Bioenzyme-responsive l-arginine-based carbon dots: the replenishment of nitric oxide for nonpharmaceutical therapy. *Biomater Sci*. 2021;9(22):7432–7443. doi:10.1039/D1BM01184G
29. Wang X, Wang W, Yu L, Tang Y, Cao J, Chen Y. Site-specific sonocatalytic tumor suppression by chemically engineered single-crystalline mesoporous titanium dioxide sonosensitizers. *J Mater Chem B*. 2017;5(24):4579–4586. doi:10.1039/C7TB00938K
30. Shi J, Chen Z, Wang B, Wang L, Lu T, Zhang Z. Reactive oxygen species-manipulated drug release from a smart envelope-type mesoporous titanium nanovehicle for tumor sonodynamic-chemotherapy. *ACS Appl Mater Interfaces*. 2015;7(51):28554–28565. doi:10.1021/acsami.5b09937
31. Qu Q, Ma X, Zhao Y. Anticancer effect of α-tocopheryl succinate delivered by mitochondria-targeted mesoporous silica nanoparticles. *ACS Appl Mater Interfaces*. 2016;8(50):34261–34269. doi:10.1021/acsami.6b13974
32. Zhao PH, Wu YL, Li XY, et al. Aggregation-enhanced sonodynamic activity of phthalocyanine–artesunate conjugates. *Angew Chem Int Ed*. 2022;61(5). doi:10.1002/anie.202113506
33. Shanei A, Akbari-Zadeh H, Fakhimikabir H, Attaran N. The role of gold nanoparticles in sonosensitization of human cervical carcinoma cell line under ultrasound irradiation: an in vitro study. Paper presented at: Journal of Nano Research; 2019.

34. Yang Y, Tu J, Yang D, Raymond JL, Roy RA, Zhang D. Photo-and sono-dynamic therapy: a review of mechanisms and considerations for pharmacological agents used in therapy incorporating light and sound. *Curr Pharm Des*. 2019;25(4):401–412. doi:10.2174/1381612825666190123114107